Applied Surface Science

Insights on the structural and electrical transport of sodium titanate nanotubes decorated with CuInS2 quantum dots heterostructures

--Manuscript Draft--

Manuscript Number:	APSUSC-D-20-07282R1
Article Type:	Full Length Article
Keywords:	CuInS2; quantum dots; titanate nanotubes; heterostructures
Corresponding Author:	Ricardo Faccio, Ph.D. Facultad de Química. Universidad de la República Montevideo, URUGUAY
First Author:	Martín Esteves
Order of Authors:	Martín Esteves
	Dominique Mombrú
	Mariano Romero
	Luciana Fernández-Werner
	Ricardo Faccio, Ph.D.
	Alvaro W. Mombrú
Abstract:	In this work we present the synthesis of nanoscale heterostructures comprising sodium titanate nanotubes $Na_2Ti_2O_5.H_2O$ (NaNT) decorated with $CuInS_2$ (CIS) quantum dots with different sizes and weight fractions. Our study focused on the structural, microstructural, electrical and optical characterization of the nanoscale heterostructure by means of high-resolution transmission electron microscopy, atomic force microscopy, grazing incidence small angle X-ray scattering, confocal Raman microscopy, UV-Vis and impedance spectroscopy analyses. In most cases, these nanoscale heterostructures exhibited considerable enhancement on the electrical conductivity explained in terms of efficient interconnections between the titanate nanotubes and CIS quantum dots. UV-Vis spectroscopy characterization showed a decrease in the optical band gap in comparison to the pure NaNT from 3.68 to 3.45 eV. Impedance spectroscopy analysis confirmed the efficient electrical interconnections between titanate nanotubes, yielding not only to a decrease in the titanate junction resistance but also to an apparent decrease in the junction barrier voltage. All these features could postulate these nanoscale heterostructures as good candidates as photoelectrodes in solar cell applications.

- Synthesis of $Na_2Ti_2O_5.H_2O$ nanotubes decorated with CIS quantum dots
- Nanoscale heterostructures directly confirmed by HRTEM and AFM.
- GI-SAXS revealed the presence of long-range correlation distances.
- Intimate contact demonstrates the presence of an apparent unique band gap.
- Improved electrical properties due to larger-sized CIS nanoparticles

Graphical Abstract (for review)

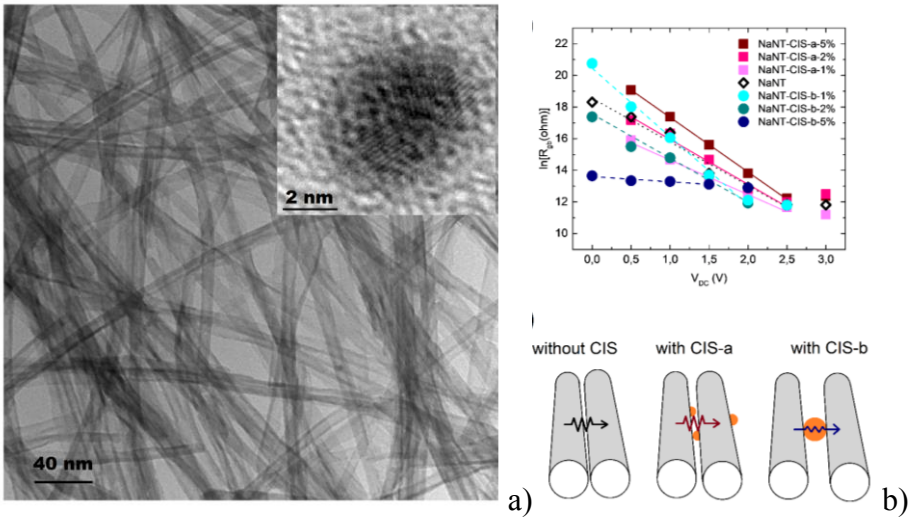

a) HRTEM images for NaNT and for CIS (inset)

b) Grain-boundary resistance dependence on the CIS-type addition.

Insights on the structural and electrical transport of sodium titanate nanotubes decorated with $CuInS_2$ quantum dots heterostructures

Martín Esteves, Dominique Mombrú, Mariano Romero, Luciana Fernández-Werner, Ricardo Faccio*, Alvaro W. Mombrú*.

Centro NanoMat/CryssMat-Lab & Grupo Física, DETEMA, Facultad de Química-Universidad de la República (UdelaR), Montevideo, CP 11800, Uruguay.

(*) Corresponding authors: rfaccio@fq.edu.uy & amombru@fq.edu.uy

Keywords: $CuInS_2$, quantum dots, titanate nanotubes, heterostructures.

Abstract

In this work we present the synthesis of nanoscale heterostructures comprising sodium titanate nanotubes $Na_2Ti_2O_5.H_2O$ (NaNT) decorated with $CuInS_2$ (CIS) quantum dots with different sizes and weight fractions. Our study focused on the structural, microstructural, electrical and optical characterization of the nanoscale heterostructure by means of high-resolution transmission electron microscopy, atomic force microscopy, grazing incidence small angle X-ray scattering, confocal Raman microscopy, UV-Vis and impedance spectroscopy analyses. In most cases, these nanoscale heterostructures exhibited considerable enhancement on the electrical conductivity explained in terms of efficient interconnections between the titanate nanotubes and CIS quantum dots. UV-Vis spectroscopy characterization showed a decrease in the optical band gap in comparison to the pure NaNT from 3.68 to 3.45 eV. Impedance spectroscopy analysis confirmed the efficient electrical interconnections between titanate nanotubes, yielding not only to a decrease in the titanate junction resistance but also to an apparent decrease in the junction barrier voltage. All these features could postulate these nanoscale heterostructures as good candidates as photoelectrodes in solar cell applications.

1. Introduction

One of the most common semiconductors utilized in solar cells is titanium dioxide, due to its wide band gap, low cost and availability. Another relevant feature lies in the dissimilarity of between conducting and valence orbitals, which helps in decreasing the electron-hole recombination[1, 2]. Additionally, different TiO_2 polymorphs have been study, considering different sizes, morphologies and aspect ratio[3-7]. TiO_2 derived one dimensional structures can be obtained by two principal methods: anodic oxidation of Ti foil and post high temperature calcination, which leads to an ordered array of TiO_2 nanotubes [8-12],, or by hydrothermal means in basic media and post washing treatments. According to the last method, sodium titanate nanotubes can be easily prepared by hydrothermal means as first reported by Kasuga *et al* [13]. These nanotubes have a layered structure with the capability of interchanging ions in between the layers during post treatment washings. They also present high superficial area and have shown interesting properties for semiconductor devices[14], and photovoltaics applications[15] among others. In particular, one-dimensional nanostructures have been in focus due to improvement in the directionality of the electron mobility and due to the decrease of the intercrystallite contacts, thus providing better electronic transport[3].

However, TiO_2, in its different polymorphs, nanostructures and titanate derived forms, presents an elevated band gap that can only be activated under UV irradiation. For this reason, these systems are often sensitized with other materials that are visible triggered [16, 17]. One strategy consists in depositing binary or ternary low band gap semiconductors such as: CdS, CdSe, PbS or CdZnTe (CZT) and $CuInS_2$ (CIS). These systems have tunable band gaps of around 1.0 to 1.5 eV and efficient multiple exciton generation, which is particularly useful in photovoltaic application [18]. Among all mentioned low band gap semiconductors, CIS is less toxic than Cd and Pb-based semiconductors. It presents high absorption coefficient, efficient multiple exciton generation and it is also a p-type semiconductor which can be turned into n-type, depending on the synthesis conditions [19]. It would be desirable to obtain a perfect p-n heterostructure on TiO_2 but it remains being a challenge to obtain a proper coverage with intimal contact. The main difficulty to get an actual p-n heterostructure is the fact that particles only locate on top of the nanotubes [20]. Nonetheless, there has been seen TiO_2-derived-CIS composites that could reach an actual p-n diode like behavior and to improve photoelectrochemical properties [21]. There are several procedures to sensitize the TiO_2-derived wide band gap semiconductor with low band gap semiconductor quantum dots (QDs). All of them can

be classified as *in-situ* or *ex-situ* techniques. For instance, chemical bath deposition (CBD), successive ionic-layer adsorption and reaction (SILAR), and electro deposition (ED) are the most common used for *in-situ* techniques [21-23]. These methods usually give a less uniform QDs distribution but higher coverage efficiency. In contrast, *ex-situ* methods present better QDs distribution but fair coverage efficiencies. In these methods, QDs are usually attached by molecular linkers, which could affect the electrical charge separation, or they can be even deposited directly on the wide band-gap semiconductor [16].

In this work, we present a facile way to synthetize nanoscale heterostructures comprising $Na_2Ti_2O_5$ nanotubes (NaNT) decorated with CIS QDs with active improvement in electrical properties, that could turn as promising materials for inorganic dye-sensitized titanate nanotubes solar cells.

2. Methods

2.1 Synthesis of sodium titanate nanotubes (NaNT)

Sodium titanate nanotubes ($Na_2Ti_2O_5 \cdot H_2O$), named as NaNT, were synthesized by a hydrothermal method. 1.25 g of TiO_2 anatase purchased from Sigma-Aldrich were dispersed on 75 mL of NaOH (10 mol/L); the reactor fill factor was set to 2/3, kept stirred at 120 rpm and heated to 145°C during 24 hs. The resulting suspension was washed several times with distilled water. The obtained solid was finally dried for 12 hours at 70°C [24].

2.2 Synthesis of $CuInS_2$ quantum dots (CIS)

$CuInS_2$ nanoparticles (CIS) were prepared by Kuo *et al.* method [25]. Briefly, 0.099 g of CuCl, 0.3040 g of thiourea and 0.2212 g of $InCl_3$ were dispersed in 80 mL of EtOH and poured into a 100 mL Teflon lined autoclave with 120 rpm stirring, and 135°C or 150°C during 6 hours. The obtained suspension was washed several times with EtOH and distilled water. The resulting solid was dried overnight at 70°C. The samples were named as CIS-T according with the synthesis temperature: T = a (for T=135°C) and T = b (for T=150°C).

2.3 Synthesis of NaNT:CIS system

A total amount of 200 mg of NaNT:CIS systems were prepared with a mixture of both components in 20 mL of EtOH and the suspension was vigorously stirred overnight until dryness. In this work we prepared the following CIS weight fraction additions: 1%, 2%, 5 % w/w, named as NaNT-CIS-T-X, with X=1, 2 and 5, respectively.

2.4 Characterizations

CIS QDs, NaNT and NaNT:CIS composite systems were studied by X-ray powder diffraction, using a Rigaku Ultima IV diffractometer, working in Bragg-Brentano configuration, under CuKα radiation, with 0.02° steps, in the 2θ range, 5.00°-100.00°. Raman spectra for all samples were collected using a WITec Alpha 300-RA equipment, working with an excitation laser wavelength of 532 and 785 nm. Atomic force microscopy in the AC mode was performed using the same equipment. Grazing incidence small angle X-ray scattering measurements (GI-SAXS) were taken using the same Rigaku Ultima IV diffractometer, with a CuKα radiation working in parallel beam configuration in the q = 0.01 – 0.10 $Å^{-1}$ range, with a fixed incident angle at 0.20° respect to the critical angle. All these procedure is in agreement with a previous methodoloy[24, 26]. The size and morphology of CIS, and NaNT:CIS samples were determined by high-resolution transmission electron microscopy (HR-TEM) employing a JEOL 2100 instrument in a 200 kV regime. Energy dispersive spectroscopy (EDS) was performed using an Oxford Instrument X-Max prob. Transmission electron microscopy (TEM) images for NaNT was obtained using a JEOL JEM 1010 with an acceleration voltage of 100 kV. Sample was dispersed in ethanol and dropped onto a carbon film supported by a copper grid. The AC impedance spectroscopy analysis was performed using a Gamry Reference 3000 impedance analyzer at T ~ 300 K. The applied AC voltage amplitude was 300 mV in the frequency range of 1 Hz – 1 MHz with applied DC voltages in the range of V_{DC}=0-5 V with 0.5 V step. Solid state reflectance measurements were carried on a UV-vis spectrophotometer Shimadzu UV-2600 with an integrating sphere in the 700 nm - 300nm range[24, 26].

3. Results and Discussion

3.1 Structural and morphological characterization

X-ray diffraction patterns (XRD) for $Na_2Ti_2O_5$ nanotubes, CIS-T (with T = a and b) and NaNT-CIS-a-5 are shown in Figure 1a and 1b, and for NaNT-CIS-a(b)-5 are shown in Figure S4. XRD profile for CIS-T, exhibited peaks at ~ 28.0°, 32.4°, 46.4°, 55.0°, 57.7°, 67.8°, 74.8° and 77.0°, assigned to (112), (020), (024), (132), (224), (040), (136) and (404) Bragg planes, respectively, associated to the presence of the Roquesite phase of CIS (JCPDS-file 00-047-1372). According to Rietveld refinement, it was possible to estimate a crystallite size domain of ~4.98 nm and 16.30 nm for CIS-a and b, respectively. Although the effect of temperature on the size and shape of CIS nanoparticles prepared by solvothermal procedures is still under debate, our results are consistent with the increase of crystallite size with increasing temperature obtained by a similar solvothermal synthesis for these CIS systems[27]. Pure NaNT XRD pattern is shown in Figure 1b: the diffraction profile presents intense peaks at ~ 9.2°, 24.0°, 28.6° and 48.3°. These four signals are assigned to (100), (011), (111) and (020) Bragg planes. On one hand, (100) is the broadest reflection and indicates that the tubes radial direction is along the **a**-axis [24, 26]. The corresponding distance associated to that reflection corresponds to the distance between [TiO_5] layers of about ~9.8 nm. It is possible to estimate a wall thickness of ~3.4 nm when using Scherrer equation. On the other hand, (020) is the narrowest signal, indicating the major coherence suggesting that the axial direction is according to **b**-axis. When applying Scherrer equation on this reflection, a crystallite size domain of 15.9 nm is obtained. According to TEM analysis, it would be indicating that the tube is mainly composed by polycrystalline domains. XRD profile for NaNT-CIS-a-5 presented the same peaks ascribed to the NaNT structure, evidencing that the nanotubes did not suffer significant changes with respect to the original structure. In this profile, the presence of the CIS is not clear because the highest peak associated with the CIS structure coincide with the highest peaks assigned to NaNT and also due to the low percentage of the CIS particles in the sample. Nevertheless, in the inset presented in the Figure 1b, the presence of a small peak at ~ 46.4° could be ascribed to the CIS structure.

High resolution transmission electron microscopy (HR-TEM) image and energy disperse spectroscopy (EDS) plot for CIS-a are shown in the Figure 2 and Figure S1, respectively. A spherical morphology with ~ 5 nm diameter is observed in the HR-TEM image for CIS quantum dots, in strong agreement with the crystallite size estimated by XRD analysis. Figure S1 also depicts the presence of copper, indium and sulfur

elements, as shown in the EDS plot. In Figure 2, the HR-TEM image for NaNT is presented, evidencing nanotubes morphology of the sample with a mean external diameter value of approximately 10 nm and a wall thickness of about 3 nm, in strong agreement with XRD analysis. The HR-TEM image for NaNT-CIS-a-5 is shown in Figure 3. In Figure 3a, CIS-a (indicated with red arrows) are observed dispersed in a NaNT matrix, and in the EDS plot (Figure S2), the presence of copper, indium and sulfur (ascribed to the CIS) and titanium, oxygen and sodium (associated with the presence of the NaNT) can be observed. In Figure 3b, HR-TEM images for NaNT-CIS-b-5 are shown, where the right-hand image is an amplification of the left-hand one. In both images, the presence of CIS quantum dots acting as an interconnection between NaNT nanotubes is clearly observed. For this case, EDS plots (Figure S3) also evidences the same behavior of the NaNT-CIS-a-5 sample, corroborating the presence of copper, indium and sulfur (ascribed to the CIS) and titanium, oxygen and sodium (associated with the presence of the NaNT).

Grazing-incidence small angle x-ray scattering (GI-SAXS) patterns for NaNT-CIS-T-X with T=a and b for different X values are shown in Figure 4. NaNT-CIS-a-X patterns showed a monotonically decrease in the intensity with increasing q, that could be associated to the presence of uncorrelated NaNT nanotubes. On the other hand, NaNT-CIS-b-X patterns presented a relative maximum at the mid-q region, that could be related with a relatively well-defined mean correlation distance (d), following $d \sim 2\pi/q_{max}$. This notorious relative maximum peak, observed at $q_{max} \sim 0.32 - 0.42$ nm^{-1} with an associated correlation distance (d) between d ~ 15–20 nm could be associated to the interspacing distance between NaNT nanotubes. The presence of this well-defined correlation length is suggesting that the CIS-b nanoparticles are probably acting as interconnectors between NaNT nanotubes, in strong agreement with HR-TEM analysis.

Raman spectra for CIS-a and CIS-b, NaNT and NaNT-CIS-a-5 are shown in Figure 5. Raman spectra for CIS-a and CIS-b were collected using a 785 nm wavelength laser and both presented a peak at ~ 365 cm^{-1}, which is in agreement with B_2 mode of $CuInS_2$[28, 29]. It is also important to mention the absence of a peak at 470 cm^{-1}, which indicates the absence of Cu_2S impurities in our samples [29]. Raman spectrum for NaNT was collected utilizing a 532 nm excitation laser and presented peaks at ~ 157, 280, 448, 704, 904 cm^{-1}; the first three are ascribed to the Ti-O-Ti vibrational modes in the TiO_5 layer [30] and

those above 700 cm^{-1} mainly attributed to the terminal Ti-O stretching mode which are reported to be sensitive to the presence of adsorbed ions [26, 31]. In the case of NaNT-CIS-a-5 spectrum (also measured utilizing a 532 nm excitation laser), exhibited practically all the peaks assigned to the NaNT, but the presence of a new peak at 370 cm^{-1} that could be ascribed to the presence of the B_2 mode of CIS. Additionally, there is a difference between the NaNT and NaNT-CIS-a-5 spectra in the 860-950 cm^{-1} region. The NaNT signal at ~ 904 cm^{-1} is splitted into two peaks at ~ 880 and 930 cm^{-1} for NaNT-CIS-a-5, suggesting a strong interaction between the surface terminal Ti-O and the CIS surface [26, 31].

The atomic force microscopy (AFM) images for NaNT, NaNT-CIS-a-5 and NaNT-CIS-b-5 are shown in the Figure 6. AFM topography analysis for NaNT shows the presence of ~ 100-200 nm size nodules with a height of ~ 10 – 50 nm which could be indicating the presence of both single and slightly aggregated NaNT nanotubes. In the NaNT-CIS-a-5 system, a different topography is observed, with the presence of nodules higher in size and height (~ 1000 - 3000 nm size and ~ 150 - 800 nm of height). On the other hand, NaNT-CIS-b-5 sample presented a similar size of nodules respect to NaNT-CIS-a-5 but with a significant lower height of ~ 30 – 50 nm. Both cases are suggesting that the presence of CIS nanoparticles causes agglomerations of NaNT, revealing a strong interaction between them.

3.2 Band gap determination

Optical gap measurements were performed on all samples by means of solid-state UV-Vis spectroscopy. Figure S5 presents the raw absorption spectra for CIS a, CIS b, NaNT, NaNT-CIS-(a)-2 and NaNT-CIS-(b)-2. At first sight it is possible to see a red shift in the absorption border for the composites. To get a better insight about the energy gaps we performed the Tauc Plots for the five cases. The obtained optical band gap for both CIS-a and CIS-b samples were 1.46 eV and 1.20 eV, respectively, as shown in Figure 7. These results are consistent with the quantum confinement effect due to the change in size of the nanoparticles evidenced in XRD and TEM analyses. Optical gap measurements for selected NaNT-CIS-(a)-2 and NaNT-CIS-(b)-2 were compared against isolated NaNT samples. For both composites, a decrease in the band gap compared to the pure NaNT was observed, from 3.68 eV to 3.60 eV for NaNT-CIS-

b-2 and to 3.45 eV for NaNT-CIS-a-2 (Figure 7) as direct band gap. This tendency could be explained in terms of band level alignments between the CIS nanoparticles and the nanotubes, so that the optical gap behaves as it is unique, but with intermediate states which results in a global red shift of the global gap. QDs of different sizes are expected to have different work functions, and consequently different alignment matching, which could explain the difference in the composites band gap values.

3.3 Electrical characterization

In order to correctly describe the complex system of the present report and obtain useful information from impedance data, we use a circuit model based in a mixed ionic-electronic conductor to explain the global charge carrier transport, as shown in **Fig. 8a**. This circuit model is based in the parallel combination of ionic and electronic resistances (R_i and R_e, respectively) together with a global geometrical capacitance (Q_{geom}), as shown in **Fig. 8a**. It is important to remark that the Q_{int} element only appears connected in series with the ionic resistance as we are working with ideal ion-blocking electrodes. In addition, we add a $R_{e,g}$–$Q_{e,gb}$ parallel combination connected in series with $R_{e,g}$ to describe the grain boundary contribution to the electronic transport in the samples [32]. In all parts of the circuit, constant phase elements (CPE) were used as non-ideal capacitors, whose impedance expression can be described by the following the equation:

$$Z_{CPE} = \frac{1}{Q(i\omega)^a}$$

where Q is the numerical value of admittance at ω = 1 rad.s^{-1}, ω is the frequency and a is an exponential factor. In the case of a = 1, the CPE resembles a capacitor and $Q = C$.[33] The larger resistance values are expected on this contribution governing almost all the electronic transport in the samples as it is associated to the inter-titanate nanotubes electronic transport. The contribution attributed to the ionic transport through the titanate structure presented the lower resistance values and are discussed thoroughly in our previous report [24]. However, it is interesting to see, that these values of R_i remain practically constant in the whole range of applied DC voltages. The second contribution (R_e) could be associated to bulk electronic transport and although its values remain relatively constant with applied DC voltages, it does not follow a marked trend and will not be discussed in detail. However, these first two processes presented the lower

resistance values respect to the third contribution ($R_{e,gb}$–$Q_{e,gb}$), which is mainly governing the overall electrical transport, as also observed for similar systems [34-37]. Nyquist plots, represented as imaginary (Z'') versus real (Z') impedance for pure NaNT samples are shown in **Fig. 8b** and NaNT-CIS-T-X are shown in **Fig. 9**. In all cases, $R_{e,gb}$ values; associated to the larger semicircle arc observed at lower frequencies, showed an exponential decrease when the applied DC voltage increases. The drop in the $R_{e,gb}$ resistance values above a certain applied DC voltage is related to the decrease in the electrical resistance since the barrier is lowered by the forward bias at the NaNT electrical junctions [38]. In the case of pure NaNT nanotubes, the major drop in the $R_{e,gb}$ resistance from ~ 12000 to 500 kohm is observed at ~ 1.5 V and could be related to a poor interconnection between NaNT nanotubes. It is interesting to note that NaNT-CIS-a-2 and NaNT-CIS-a-5 showed higher $R_{e,gb}$ values (~ 30000 kohm) than pure NaNT titanate nanotubes at DC voltages below ~ 1.5 V until it drops to similar values (~ 200 – 500 kohm) above ~ 1.5 V. Nevertheless, NaNT-CIS-a-1, NaNT-CIS-b-1, NaNT-CIS-b-2 and NaNT-CIS-b-5 samples showed lower $R_{e,gb}$ values in comparison to NaNT nanotubes, in practically the entire voltage regime with the only exception that NaNT-CIS-b-5 showed a crossover to slightly higher values above 1.5 V. In addition, NaNT-CIS-b-1, NaNT-CIS-b-2 and NaNT-CIS-b-5 samples, which are the ones with larger-sized CIS nanoparticles, yielded to a drop in the $R_{e,gb}$ resistance at lower DC voltages. In order have more insight on the exponential decay in the $R_{e,gb}$ resistance values, a typical charge injection model of a semiconductor heterojunction can be used. Under dark conditions, $R_{e,gb}$ followed a characteristic exponential dependence with the applied bias, which is consistent with the expression:

$$R = R_0 exp\left(-\frac{q\Delta V}{nk_B T}\right)$$

where R_0 is a constant and n is a dimensionless parameter[39]. The linearization of the grain boundary resistance ($R_{e,gb}$) versus applied DC voltage for all cases is shown in **Fig. 10**. For NaNT-CISa-X samples, good linearity is observed up to 2.5 V and a decrease of both $R_{e,gb}$ and slope for X=1% while an increase of both $R_{e,gb}$ and slope for X=5% are observed, respect to pure NaNT. For NaNT-CISb-X samples, good linearity is observed up to 1.5–2.0 V and an increase of both $R_{e,gb}$ and slope for X=1% while an decrease in both $R_{e,gb}$ and slope for X=5% are observed, respect to pure NaNT. Based in

these results, we can conclude that NaNT with lower-sized CIS quantum dots (CISa) heterostructures only yield an enhancement on the electronic transport at lower CIS concentrations. On the other hand, NaNT with larger-sized CIS quantum dots (CISb) heterostructures yielded drastic enhancement on the electronic transport at higher CIS concentrations. It is possible that the strong electrical conductivity dependence with different CIS concentration obeys purely to percolation effects. However, it is also evident that the strong electrical conductivity dependence with different CIS mean sizes is rather relevant suggesting that larger CIS quantum dots probably exhibit less resistive interphases with NaNT. This is suggesting that the presence of larger-sized CIS nanoparticles is probably acting as better interconnectors between titanate nanotubes, yielding not only to a decrease in the titanate junction resistance but also to an apparent decrease in the junction barrier voltage.

4. Conclusions

We report the successful synthesis of $Na_2Ti_2O_5.H_2O$ nanotubes decorated with $CuInS_2$ quantum dots. The presence of nanoscale heterostructures were directly confirmed by HRTEM, while AFM and GI-SAXS revealed the presence of long-range correlation distances in agreement with the successful formation of the heterojunction, especially when larger CIS quantum dots are present. It turns out that intimate contact between CIS and NaNT yielded to the presence of an apparent unique band gap which is decreased respect to the NaNT pure nanotubes. Finally, the system also presented an improvement on the electrical properties evidencing that the presence of larger-sized CIS nanoparticles is probably acting as better interconnectors between titanate nanotubes, yielding not only to a decrease in the titanate junction resistance but also to an apparent decrease in the junction barrier voltage. For all these reasons we propose NaNT-CIS-b composites as materials with potential interest as photoelectrode in solar cells applications.

Acknowledgments

The authors wish to thank the Uruguayan CSIC, ANII and PEDECIBA funding institutions. In addition, we would like to thank technical support of Alvaro Olivera and

the collaboration of Laura Fornaro at GDMEACURE high-resolution transmission electron microscopy laboratory.

References

1. R. Faccio, L. Fernández-Werner, H. Pardo and A. W Mombru, *Recent patents on nanotechnology*, 2011, **5**, 46-61.
2. R. Jose, V. Thavasi and S. Ramakrishna, *Journal of the American Ceramic Society*, 2009, **92**, 289-301.
3. C. C. Raj and R. Prasanth, *Journal of Power Sources*, 2016, **317**, 120-132.
4. J. Yang, S. Mei and J. Ferreira, *Materials Science and Engineering: C*, 2001, **15**, 183-185.
5. T. Sugimoto, X. Zhou and A. Muramatsu, *Journal of Colloid and Interface Science*, 2003, **259**, 53-61.
6. M. Wang, J. Bai, F. Le Formal, S.-J. Moon, L. Cevey-Ha, R. Humphry-Baker, C. Grätzel, S. M. Zakeeruddin and M. Grätzel, *The Journal of Physical Chemistry C*, 2012, **116**, 3266-3273.
7. D. V. Bavykin, V. N. Parmon, A. A. Lapkin and F. C. Walsh, *Journal of Materials Chemistry*, 2004, **14**, 3370-3377.
8. Z. Liu, Q. Wang, X. Tan, S. Zheng, H. Zhang, Y. Wang and S. Gao, *Journal of Alloys and Compounds*, 2020, **815**, 152478.
9. D. Cao, Q. Wang, Y. Wu, S. Zhu, Y. Jia and R. Wang, *Separation and Purification Technology*, 2020, 117132.
10. Z. Liu, Y. Song, Q. Wang, Y. Jia, X. Tan, X. Du and S. Gao, *Journal of colloid and interface science*, 2019, **556**, 92-101.
11. Q. Wang, H. Li, X. Yu, Y. Jia, Y. Chang and S. Gao, *Electrochimica Acta*, 2020, **330**, 135167.
12. Y. Wang, Q. Wang, H. Zhang, Y. Wu, Y. Jia, R. Jin and S. Gao, *Separation and Purification Technology*, 2020, 116775.
13. T. Kasuga, M. Hiramatsu, A. Hoson, T. Sekino and K. Niihara, *Langmuir*, 1998, **14**, 3160-3163.
14. K. Vinodgopal, S. Hotchandani and P. V. Kamat, *The Journal of Physical Chemistry*, 1993, **97**, 9040-9044.
15. X.-L. Sui, Z.-B. Wang, C.-Z. Li, J.-J. Zhang, L. Zhao and D.-M. Gu, *Journal of Power Sources*, 2014, **272**, 196-202.
16. A. Salant, M. Shalom, I. Hod, A. Faust, A. Zaban and U. Banin, *Acs Nano*, 2010, **4**, 5962-5968.
17. B. Li, L. Wang, B. Kang, P. Wang and Y. Qiu, *Solar energy materials and solar cells*, 2006, **90**, 549-573.
18. M. Booth, A. P. Brown, S. D. Evans and K. Critchley, *Chemistry of Materials*, 2012, **24**, 2064-2070.
19. T. Yukawa, K. Kuwabara and K. Koumoto, *Thin Solid Films*, 1996, **286**, 151-153.
20. R. Liu, Y. Liu, C. Liu, S. Luo, Y. Teng, L. Yang, R. Yang and Q. Cai, *Journal of Alloys and Compounds*, 2011, **509**, 2434-2440.
21. J.-H. Yun, Y. H. Ng, S. Huang, G. Conibeer and R. Amal, *Chemical Communications*, 2011, **47**, 11288-11290.
22. S. Gorer and G. Hodes, *The Journal of Physical Chemistry*, 1994, **98**, 5338-5346.
23. H. Lee, M. Wang, P. Chen, D. R. Gamelin, S. M. Zakeeruddin, M. Gratzel and M. K. Nazeeruddin, *Nano letters*, 2009, **9**, 4221-4227.

24. M. Esteves, L. Fernández-Werner, F. Pignanelli, M. Romero, M. R. Chialanza, R. Faccio and Á. W. Mombrú, *Ceramics International*, 2019.
25. K.-T. Kuo, D.-M. Liu, S.-Y. Chen and C.-C. Lin, *Journal of Materials Chemistry*, 2009, **19**, 6780-6788.
26. M. Esteves, L. Fernández-Werner, F. Pignanelli, B. Montenegro, M. Belluzzi, M. Pistón, M. R. Chialanza, R. Faccio and Á. W. Mombrú, *Ceramics International*, 2019, **45**, 708-717.
27. J. Benbelgacem, A. B. Marai, R. Mendil, K. Medjnoun, K. Djessas and Z. B. Ayadi, *Journal of Alloys and Compounds*, 2017, **692**, 966-971.
28. E. Dutková, M. J. Sayagués, J. Briančin, A. Zorkovská, Z. Bujňáková, J. Kováč, P. Baláž and J. Ficeriová, *Journal of materials science*, 2016, **51**, 1978-1984.
29. V. Dzhagan, B. Kempken, M. Valakh, J. Parisi, J. Kolny-Olesiak and D. R. Zahn, *Applied Surface Science*, 2017, **395**, 24-28.
30. E. German, R. Faccio and Á. W. Mombrú, *Applied Surface Science*, 2017, **426**, 1182-1189.
31. B. C. Viana, O. P. Ferreira, A. G. Souza Filho, A. A. Hidalgo, J. Mendes Filho and O. L. Alves, *Vibrational Spectroscopy*, 2011, **55**, 183-187.
32. R. A. Huggins, *Ionics*, 2002, **8**, 300-313.
33. J. T. Irvine, D. C. Sinclair and A. R. West, *Advanced materials*, 1990, **2**, 132-138.
34. C. Yim, N. McEvoy, H.-Y. Kim, E. Rezvani and G. S. Duesberg, *ACS applied materials & interfaces*, 2013, **5**, 6951-6958.
35. P. Ilaiyaraja, B. Rakesh, T. K. Das, P. S. Mocherla and C. Sudakar, *Solar Energy Materials and Solar Cells*, 2018, **178**, 208-222.
36. J.-Y. Chang, J.-M. Lin, L.-F. Su and C.-F. Chang, *ACS applied materials & interfaces*, 2013, **5**, 8740-8752.
37. B. R. Sankapal, D. B. Salunkhe, S. Majumder and D. P. Dubal, *RSC Advances*, 2016, **6**, 83175-83184.
38. V. González-Pedro, X. Xu, I. Mora-Sero and J. Bisquert, *ACS nano*, 2010, **4**, 5783-5790.
39. S. M. Sze and K. K. Ng, *Physics of semiconductor devices*, John wiley & sons, 2006.

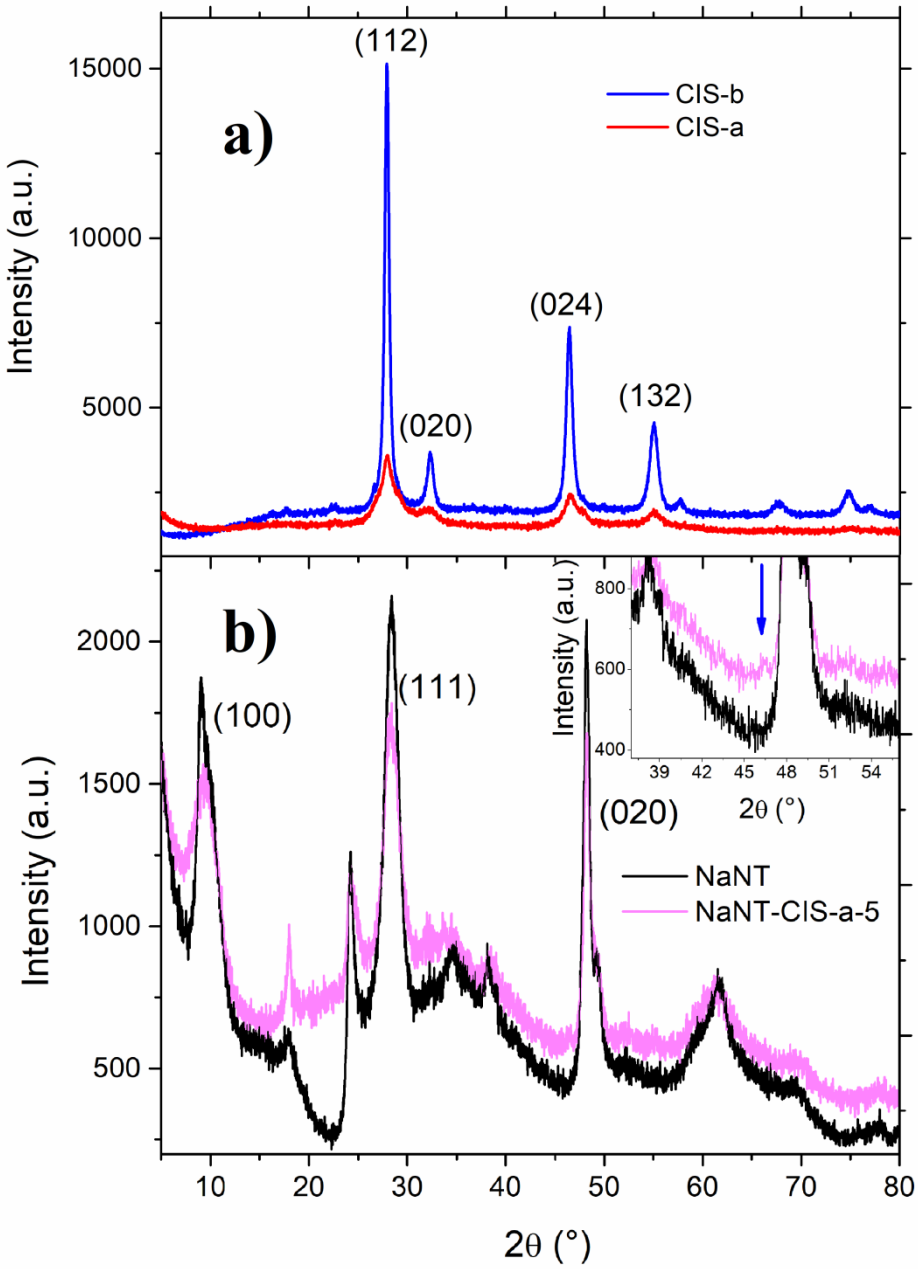

Figure 1 –XRD patterns for a) CIS-a and CIS-b and b) NaNT and NaNT-CIS-a-5.

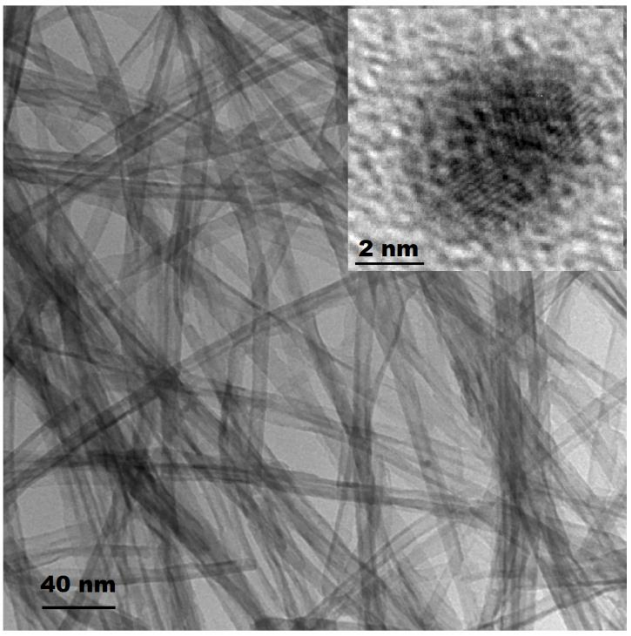

Figure 2 –HR-TEM images for NaNT and in the inset for CIS-a.

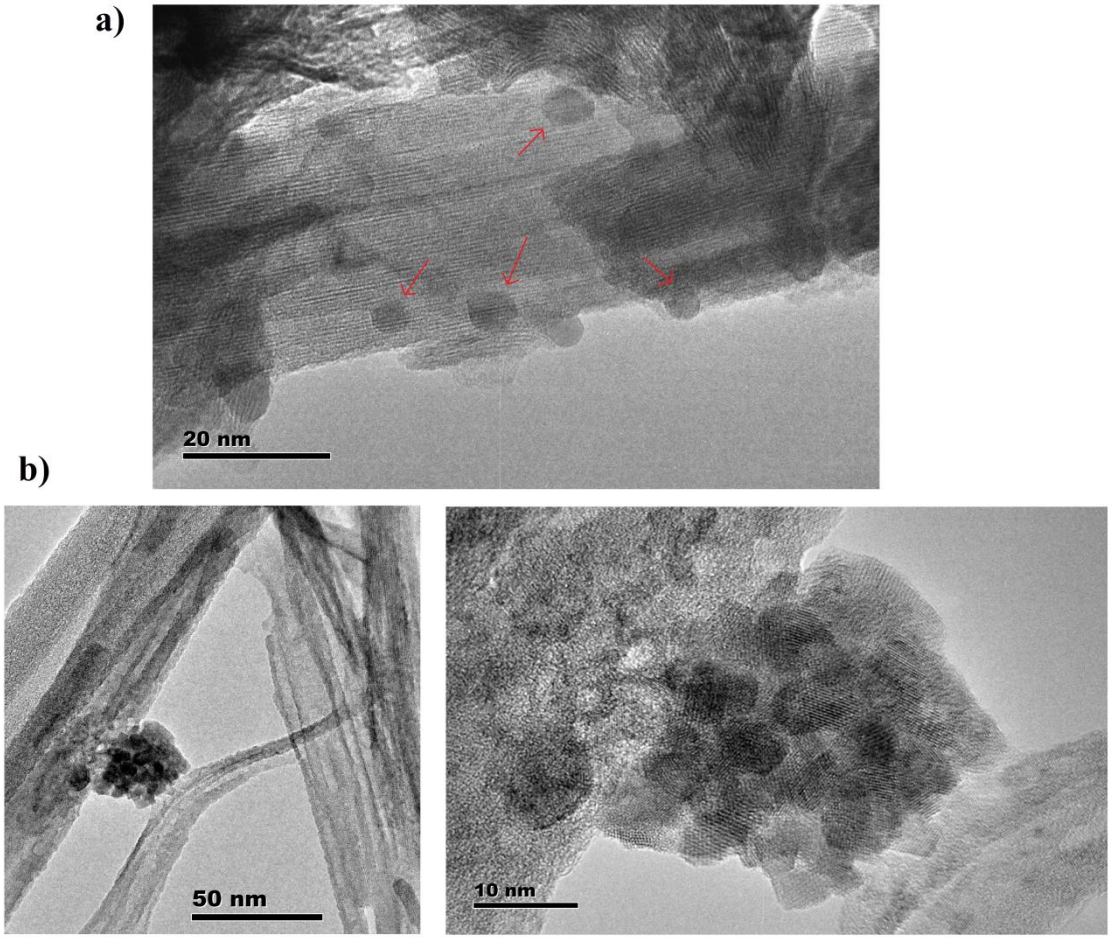

Figure 3 – HR-TEM image for a) NaNT-CIS-a-5 and b) NaNT-CIS-b-5. The presence of CIS-a quantum dots is indicated with red arrows.

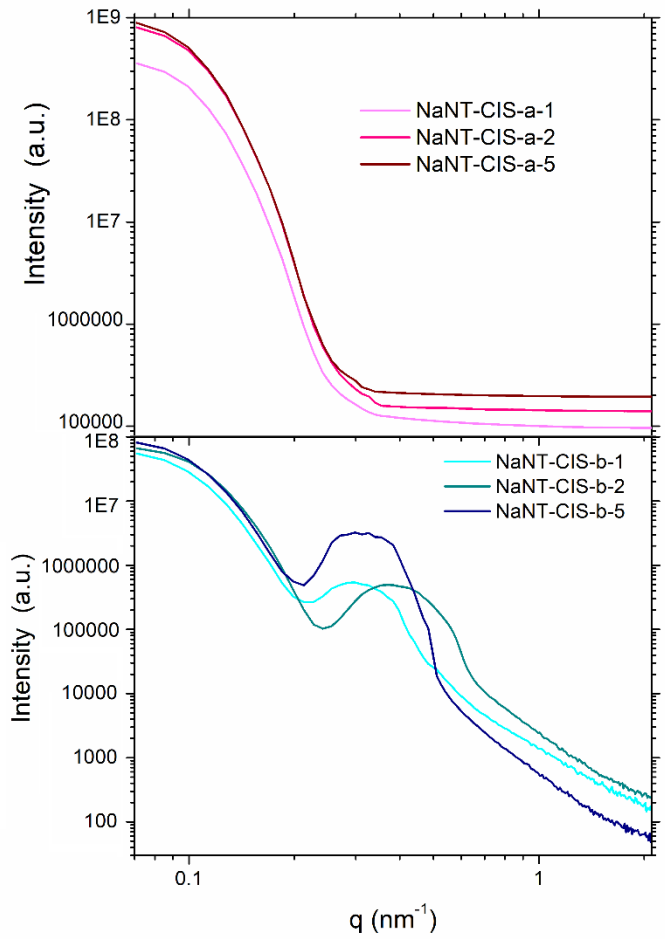

Figure 4 – GI-SAXS analysis for NaNT-CIS-a (upper panel) and NaNT-CIS-b (lower panel) samples.

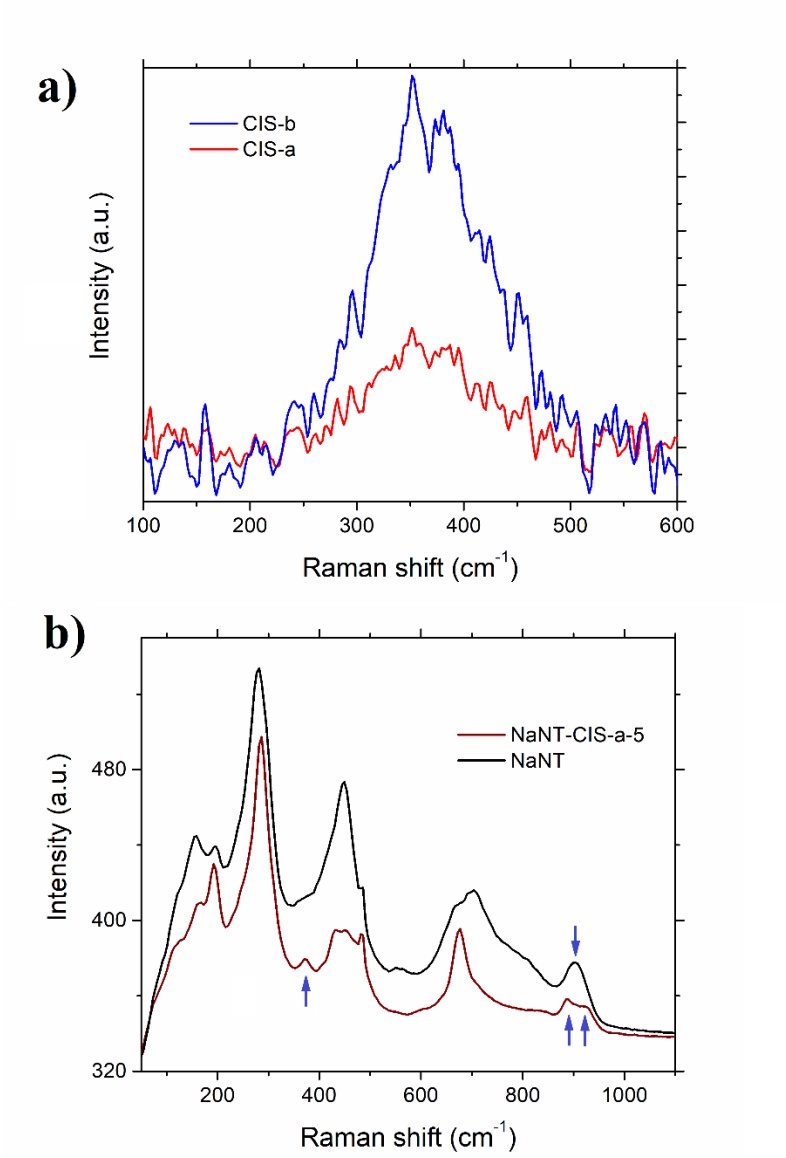

Figure 5 – Raman spectra for a) CIS-a and CIS-b, b) NaNT and NaNT-CIS-a-5.

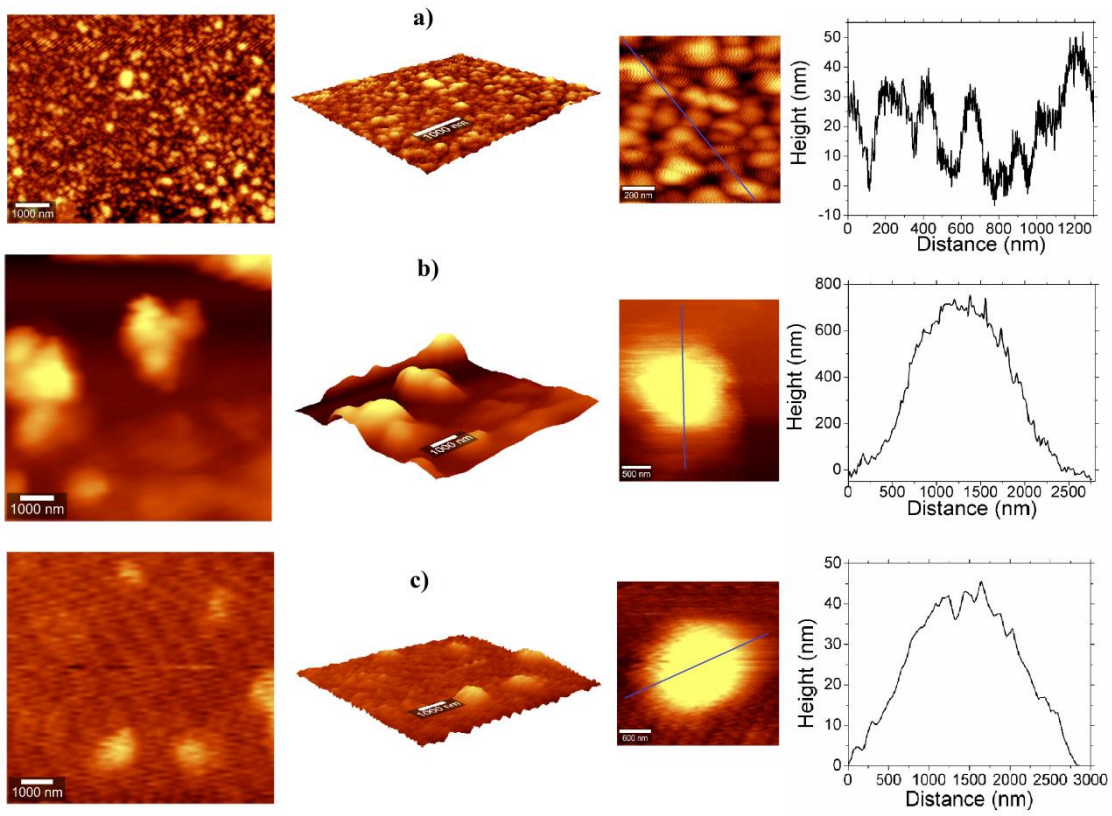

Figure 6 – AFM images for a) NaNT, b) NaNT-CIS-a-5 and c) NaNT-CIS-b-5. The graphics on the right side corresponds with the cross-section marked in the next image.

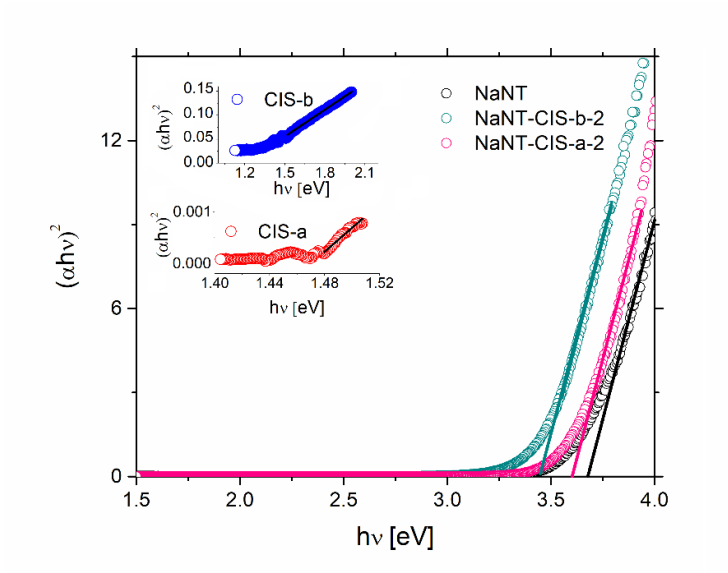

Figure 7-Tauc plots for CIS-a(b), NaNT and NaNT-CIS-a(b)2 composites.

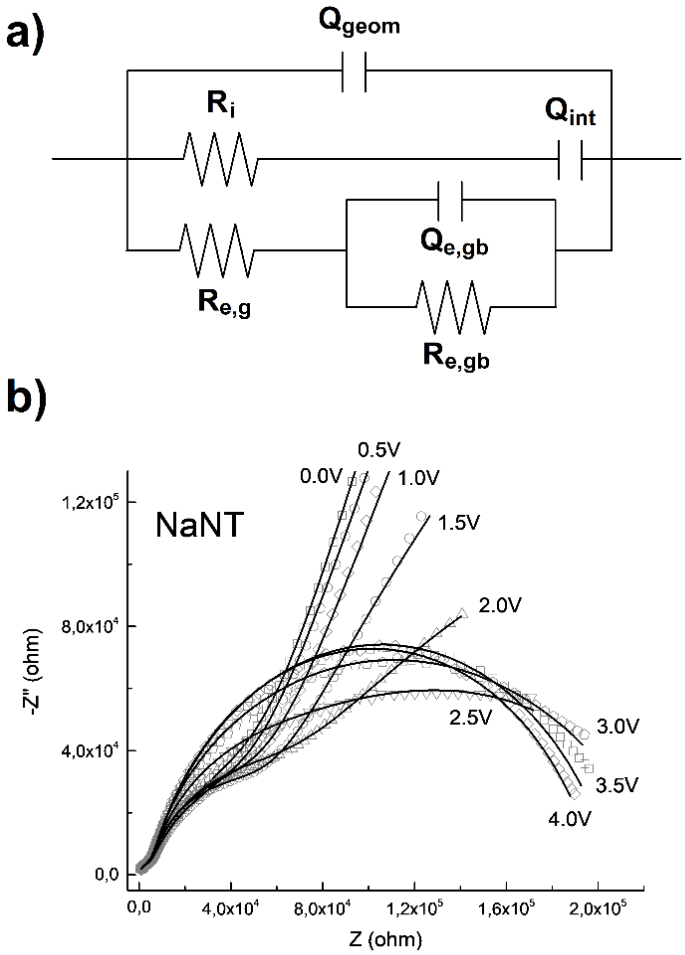

Figure 8 – **a**) Equivalent circuit model and **b**) Nyquist plots as a function of different applied DC selected voltages ranged between V_{DC} = 0 – 4 V for NaNT.

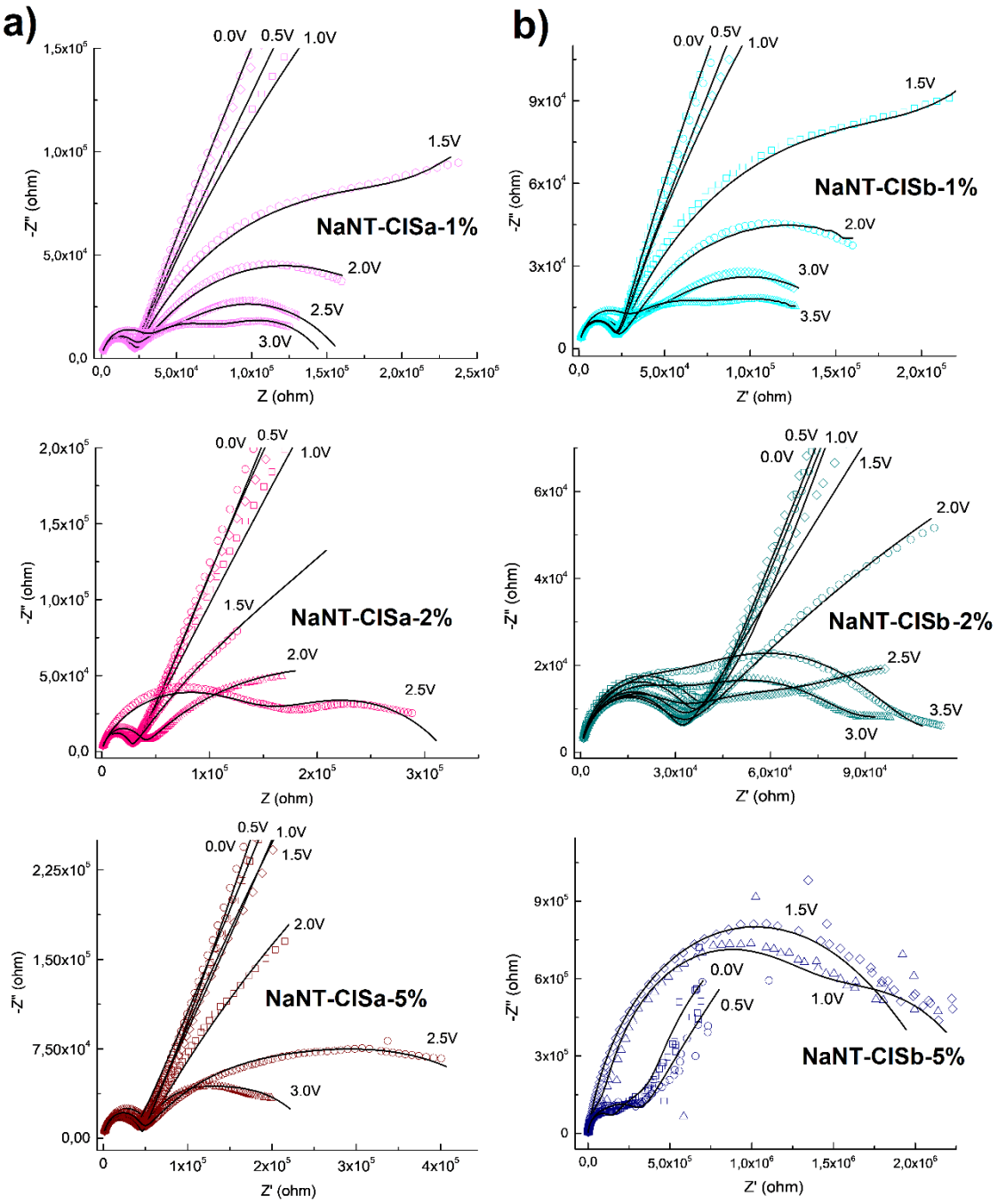

Figure 9 – Nyquist plots as a function of different applied DC selected voltages ranged between V_{DC} = 0 – 3 V for **a**) NaNT-CIS-a-X and **b**) NaNT-CIS-b-X with X = 1, 2 and 5%.

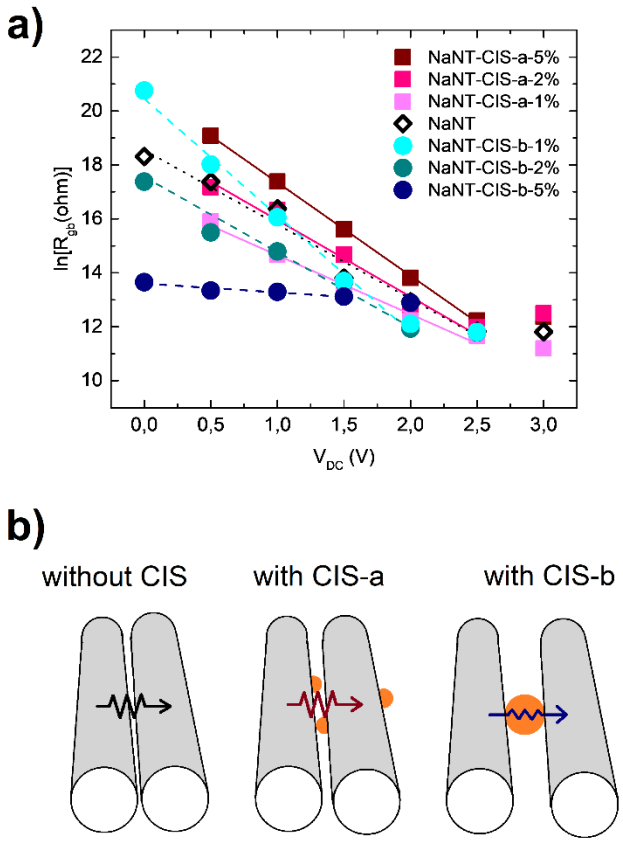

Figure 10 – a) Linearization of the grain boundary resistance ($R_{e,gb}$) versus applied DC voltage for and **b**) schematization of structural and electrical insights for NaNT without CIS, decorated with lower-sized quantum dots (CIS-a) and larger-sized CIS quantum dots (CIS-b).

Credit Author Statement

Martín Esteves & Dominique Mombrú: Methodology, Data curation and Writing- Original draft preparation. **Mariano Romero & Luciana Fernández-Werner**: Supervision and Data Curation. **Ricardo Faccio and Alvaro W. Mombrú**: Conceptualization, Writing- Reviewing and Editing.